CHEMISTRY OF MATERIALS

ARTICLE

pubs.acs.org/cm

# Long-Range and Local Structure in the Layered Oxide $Li_{1.2}Co_{0.4}Mn_{0.4}O_2$†

J. Bareño,[‡] M. Balasubramanian,[*,§] S. H. Kang,[‡] J. G. Wen,[⊥] C. H. Lei,[⊥] S. V. Pol,[§] I. Petrov,[⊥] and D. P. Abraham[*,‡]

[‡]Chemical Sciences and Engineering Division, Argonne National Laboratory, 9700 S. Cass Avenue, Argonne, Illinois 60439, United States

[§]Advanced Photon Source, Argonne National Laboratory, 9700 S. Cass Avenue, Argonne, Illinois 60439, United States

[⊥]Frederick Seitz Materials Research Laboratory, University of Illinois, 104 S. Goodwin Avenue, Urbana, Illinois 61801, United States

Supporting Information

**ABSTRACT:** The layered oxides being considered as intercalation compounds for lithium batteries display significant differences between the long-range crystal structure and local arrangements around individual atoms. These differences are important, because the local atomic environments affect Li-ion transport and, hence, the oxide's rate capability, by determining activation barrier energies, by blocking or opening Li-diffusion pathways, etc. Traditional diffraction methods provide key information on the average crystal structure. However, no single experimental technique can unequivocally determine the average long-range crystal structure and the distribution of local environments over crystallographic distances while retaining atomic-scale resolution. Therefore, in this study, we have employed a combination of diffraction, microscopy, and spectroscopy techniques to investigate the long-range (~1 $\mu$m) and local structure (≤1 nm) of $Li_{1.2}Co_{0.4}Mn_{0.4}O_2$, which is a model compound for layered oxides being considered for transportation applications. We find that $Li_{1.2}Co_{0.4}Mn_{0.4}O_2$ contains mostly $Mn^{4+}$ in $Li_2MnO_3$-like atomic environments and $Co^{3+}$ in $LiCoO_2$-like atomic environments, which are intimately mixed over length scales of ≥2−3 nm, resulting in a $Li_{1.2}Co_{0.4}Mn_{0.4}O_2$ crystallite composition that appears homogeneous over the long-range. In addition, we observed a quasi-random distribution of locally monoclinic structures, topotaxially integrated within a rhombohedral-$NaFeO_2$ framework. Based on these observations, we propose a dendritic microstructure model for $Li_{1.2}Co_{0.4}Mn_{0.4}O_2$ consisting of well integrated $LiCoO_2$- and $Li_2MnO_3$-like structures.

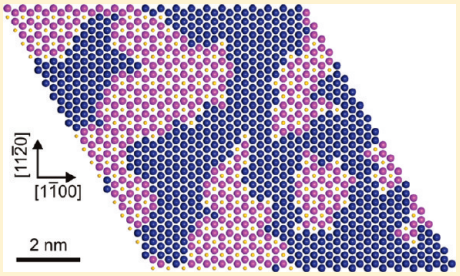


**KEYWORDS:** lithium-ion batteries, XRD, XAS, TEM

## INTRODUCTION

The arrangement of atoms in the crystal lattice determines the physical, chemical, thermal, and mechanical properties of materials. In pure compounds and elemental crystals, every atom is located on a periodic lattice array, especially at low temperatures, to reduce the total energy of the system. Lattice parameters of the periodic array are typically determined by diffraction techniques, such as X-ray diffraction (XRD). In single-phase binary alloys of isostructural materials, the lattice parameters are seen to vary linearly with the composition of its end members (Vegard's law). Therefore, the constituent atoms may be assumed to occupy lattice sites in the composition-averaged structure, an approach central to the virtual crystal approximation (VCA) often employed in *ab initio* studies of alloy mixtures.

In real materials, however, the constituent atoms may not sit at the VCA sites. Atomic size differences, relaxations around defects, and the tendency for like or unlike atoms to cluster can all induce local lattice distortions, while preserving the long-range periodicity of the overall structure. These local lattice distortions are typically characterized by extended X-ray absorption fine structure (EXAFS) measurements, which are well-suited for the determination of nearest-neighbor spacing in crystal structures.[1−3] For example, in $Ga_{1-x}In_xAs$ solid solutions ($x$ = 0−1), the changes in the average cation−anion distance determined via XRD follow Vegard's law, whereas the actual nearest-neighbor spacings (Ga−As, In−As) determined by EXAFS remain almost constant across the solid solutions. That is, while the long-range structure in $Ga_{1-x}In_xAs$ shows periodic variations with $x$ in the XRD data, the local structure around the cations (Ga, In) exhibits significant deviations from the periodicity. This apparent discrepancy arises because Bragg peaks in XRD patterns appear at positions determined by the composition-averaged structure and, hence, provide long-range information, whereas EXAFS provides short-range information on the crystal structure.

The layered oxides that are being considered as positive electrode intercalation compounds for lithium batteries also display significant differences between the long-range crystal structure and local arrangements around individual atoms. Among these oxides, the structure−electrochemical-property relationships in $LiCoO_2$, $LiNiO_2$, and $LiNi_{1-y}Co_yO_2$ samples have been investigated

**Received:** August 19, 2010
**Revised:** March 11, 2011
**Published:** March 25, 2011

ACS Publications © 2011 American Chemical Society

extensively.[4−11] XRD studies have indicated that these compounds have, in a general sense, a layered α-$NaFeO_2$-type structure ($R\bar{3}m$ symmetry) in which the Na sites are occupied by Li and the Fe sites are occupied by transition-metal (TM) ions, albeit with some degree of interchange between atoms in the Li and Ni layers of $LiNiO_2$. However, EXAFS measurements around the Ni atom in nearly stoichiometric $LiNiO_2$ show local lattice distortions; the Ni is coordinated with four O atoms at a distance of 1.92 Å and two O atoms at 2.08 Å.[12] This distorted octahedral coordination has been ascribed to a noncooperative Jahn−Teller (JT) effect, which is specific to $Ni^{3+}$ in the low-spin state, where the oxygen octahedra about $Ni^{3+}$ are distorted but not aligned throughout the sample.[13] Similar local lattice distortions have also been reported in various $LiNi_{1-y}Co_yO_2$ samples, although the corresponding XRD data show no evidence of long-range lattice distortions. For example, in $LiNi_{0.85}Co_{0.15}O_2$,[11] the Ni−O octahedra are distorted (four Ni−O at 1.91 Å, two Ni−O at 2.04 Å) according to the JT distortion expected for $Ni^{3+}$; however, the Co−O octahedra are symmetric (1.91 Å), indicating the presence of the JT-inactive $Co^{3+}$ ion. The size and shape differences between the Ni−O and Co−O octahedra induce additional local distortions in the crystal structure. These distortions in the TM−O octahedra are of consequence because they induce distortions in the associated Li−O octahedra, which, in turn, affect Li-ion motion and, hence, the electrochemical properties of the oxide.

In addition to lattice distortions, other effects, such as charge ordering,[14−16] clustering tendencies,[17] and orbital ordering,[13] may serve to reduce the overall energy of the system and overcome the configuration entropy contribution that serves to randomize the distribution of cations in these oxides. For example, $Li^{1+}$−$Mn^{4+}$ charge ordering is known to occur in the TM planes of $Li_2MnO_3$ (= $Li[Li_{0.33}Mn_{0.66}]O_2$); scanning transmission electron microscopy (STEM) images of $Li_2MnO_3$[18] show six $Mn^{4+}$ around each $Li^+$, resulting in a $\sqrt{3} \times \sqrt{3} - R30°$ reconstruction in the TM plane that produces a tessellation of edge-sharing $LiMn_6$ hexagonal units.[18] Furthermore, the relative stacking of TM planes within the layered rock salt parent structure, aligning Li cations across successive TM planes, produces the monoclinic $C2/m$ structure.[18−21] $Ni^{2+}$−$Mn^{4+}$ charge ordering also plays a role in the TM planes of $NaNi_{0.5}Mn_{0.5}O_2$ and $LiNi_{0.5}Mn_{0.5}O_2$ (prepared from $NaNi_{0.5}Mn_{0.5}O_2$ by an ion-exchange process), as claimed by Bréger et al,.[22] using nuclear magnetic resonance (NMR) spectroscopy and neutron pair distribution function (PDF) analysis, associated with reverse Monte Carlo (RMC) calculations. For both compounds, one could expect both Ni and Mn to be in the +3 oxidation state, in which both ions are Jahn−Teller active. However, instead of undergoing a Jahn−Teller distortion, the ions relax to $Ni^{2+}$ and $Mn^{4+}$ and order, forming alternating zigzag rows along the $[1\bar{1}00]$ directions in the TM planes. In $LiNi_{0.5}Mn_{0.5}O_2$, the $Ni^{2+}$−$Mn^{4+}$ and $Li^{1+}$−$Mn^{4+}$ correlations suppress the $Mn^{4+}$−$Mn^{4+}$ correlations, which are the least favorable energetically. Similarly, in $Li_2MnO_3$, $Li^{1+}$−$Mn^{4+}$ correlations are favored energetically over $Mn^{4+}$−$Mn^{4+}$ correlations.

Evidence of elemental clustering, forming local $Li_2MnO_3$-like and $LiCrO_2$-like environments in the TM planes, has been reported in as-prepared $Li_{1.2}Cr_{0.4}Mn_{0.4}O_2$.[23] EXAFS analysis of $Li_{1.2}Cr_{0.4}Mn_{0.4}O_2$ revealed that the atomic environment about Cr contains six first O neighbors at 1.97 Å and six metal (Cr and/or Mn) atoms at 2.89 Å, in good agreement with both a layered rock salt structure and the expected $Cr^{3+}$−O bond in octahedrally coordinated compounds. In addition, the atomic environment about Mn consists of six O neighbors at 1.89 Å and four metal neighbors at 2.87 Å, in good agreement with coordination values and the Mn−O bond distance (1.90 Å) expected for $Mn^{4+}$ cations in $Li_2MnO_3$. In $Li_{1.2}Cr_{0.4}Mn_{0.4}O_2$, the screened columbic repulsion between $Cr^{3+}$−$Mn^{4+}$ and $Mn^{4+}$−$Mn^{4+}$ would be greater than that between $Li^{1+}$−$Mn^{4+}$ and $Cr^{3+}$−$Cr^{3+}$ correlations. Therefore, assuming that charge ordering energetics play a role, local clustering into $Li_2MnO_3$-like and $LiCrO_2$-like regions can be expected, driven primarily by the lower energy penalty in forming the $Li^{1+}$−$Mn^{4+}$ correlations.

The local atomic structure, rather than the average long-range structure, governs properties such as activation barriers, strain fields, and steric hindrances that affect Li-ion transport in these layered oxides and, hence, their performance during electrochemical cycling.[24−26] In this article, we employ $Li_{1.2}Co_{0.4}Mn_{0.4}O_2$, which may be described as $0.5Li_2MnO_3 \cdot 0.5LiCoO_2$ in two-component notation,[27] as a model compound to study the structure of $Li_{1+x}(Ni_aCo_bMn_c)_{1-x}O_2$ materials being considered for plug-in hybrid electric vehicle applications. We chose $Li_{1.2}Co_{0.4}Mn_{0.4}O_2$ because the similarity of the M−O (1.91 vs 1.90 Å) and M−M (2.82 vs 2.85 Å) bond lengths in $LiCoO_2$ and $Li_2MnO_3$, respectively, results in a much lower contribution of bond strain relaxation to static disorder and, consequently, improved accuracy of the EXAFS analysis.

We build upon our recent analytical electron microscopy (AEM) study of $Li_{1.2}Co_{0.4}Mn_{0.4}O_2$,[28] complementing it with a combination of techniques including scanning electron microscopy (SEM), XRD, X-ray absorption spectroscopy (XAS), and electrochemical cycling, in order to investigate the long-range and local structure of $Li_{1.2}Co_{0.4}Mn_{0.4}O_2$. These techniques provide information on oxide morphology (via SEM), long-range structure (via XRD), oxidation states and local structure (few coordination shells) of the TM atoms (via XAS), and crystal structures and ordering in the TM planes (via AEM). Studies of this nature are intended to provide fundamental structural insights on layered oxides that are needed to develop transformational materials with high capacities, high power, and stable crystal structures for Li-battery applications.

## 2. EXPERIMENTAL SECTION

$Li_{1.2}Co_{0.4}Mn_{0.4}O_2$ was synthesized from stoichiometric amounts of $Li_2CO_3$ and $(Co_{0.5}Mn_{0.5})CO_3$ precursors that were thoroughly mixed and calcined at 900 °C for 12 h in air. To compensate for possible lithium loss during the high-temperature calcination, a small excess of lithium (2 at.%) was used during sample synthesis. Electrodes for electrochemistry experiments were prepared by coating an aluminum foil with a mixture containing $Li_{1.2}Co_{0.4}Mn_{0.4}O_2$, SFG-6 graphite, acetylene black, and polyvinylidene fluoride (PVDF) binder (84:4:4:8 by weight).

SEM analysis of the electrodes was conducted using a high-resolution Hitachi Model S-4700 microscope with a field-emission electron source. XRD data were collected on a Philips powder X-ray diffractometer, using Cu Kα radiation for $2\theta$ values in the range of 10°−80°. XAS experiments were performed in the PNC-XSD bending magnet beamline (20-BM) of the Advanced Photon Source at Argonne National Laboratory. Measurements at the Mn and Co K-edges were performed in the transmission mode using gas ionization chambers to monitor the incident and transmitted X-ray intensities. A pair of Si(111) crystals was used to monochromatize the radiation. A rhodium-coated X-ray mirror was used to suppress higher-order harmonics. Energy calibration was carried out using the first inflection point of the spectrum of the appropriate metal foil.[29]

Transmission electron microscopy (TEM) samples were prepared by punching a 3-mm disk from the coated electrode. The disk was

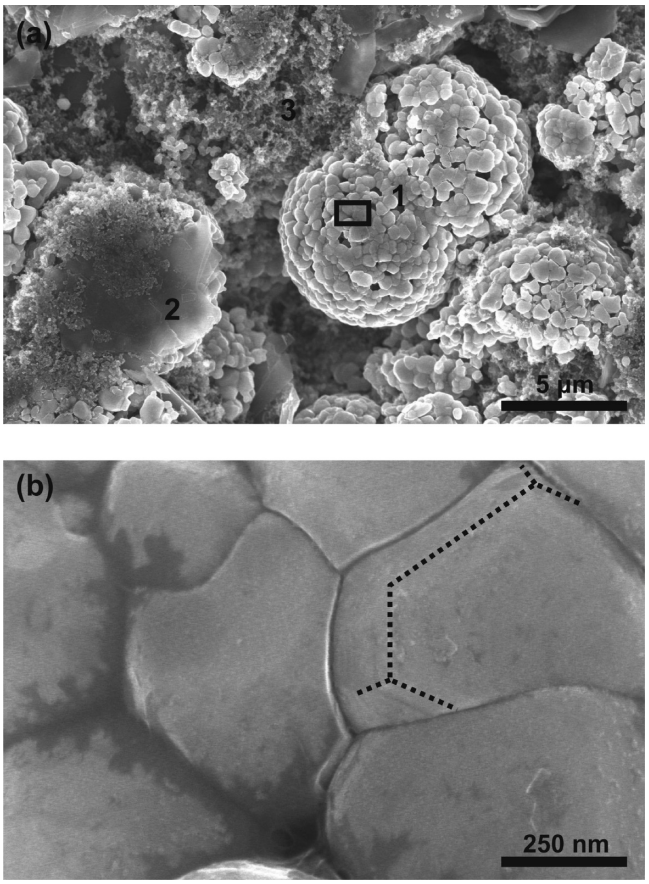


**Figure 1.** (a) Electrode SEM image showing (1) $Li_{1.2}Co_{0.4}Mn_{0.4}O_2$, (2) graphite, and (3) acetylene black. (b) Magnified view of the area marked by a box in panel a, showing primary $Li_{1.2}Co_{0.4}Mn_{0.4}O_2$ particles. Dotted lines highlight facets within a primary particle.

subsequently glued (coating side) onto a copper ring and the aluminum foil was gently removed, leaving only the electrode coating on the copper ring. The sample was then Ar-ion-milled from both sides at an ion energy of 5 kV and low-incidence angle (6°) for 30 min, followed by further milling for ~30 min at 3 kV to perforation. The ion-milled TEM sample, which was cooled with liquid nitrogen during the milling process, provided large electron transparent areas containing many oxide particles suitable for crystal structure examination. Another set of TEM samples was prepared by scratching off the electrode coating from the Al foil and hand crushing the resulting powder with a mortar and pestle in a menthol dispersion. The oxide suspension was then placed onto a holey carbon grid for TEM observation.

Lattice-resolution TEM and selected-area electron diffraction (SAED) studies were carried out at 200 kV with a JEOL Model 2010LaB$_6$ instrument. The samples were tilted in the microscope to examine the crystal structure along various zone axes, and experimental SAED patterns were compared to WebEMAPS[30] simulations to assist interpretation. High-angle annular dark-field (HAADF) STEM images were acquired using a JEOL Model 2200FS instrument equipped with a probe aberration corrector (CEOS GmbH, Heidelberg, Germany). The lateral resolution of the JEOL 2200FS instrument for HAADF imaging is ~0.1 nm. HAADF STEM, which is a high-angle (~100 mrad) annular detector, is used to collect incoherently scattered electrons while a narrow beam is scanned over the specimen. Because the intensity recorded by the HAADF detector is dominated by incoherent electron scattering rather than by Bragg diffraction, the resulting pixel intensity is proportional to $Z^n$, where $n \simeq 2$ and $Z$ is the mean atomic number of the specimen area being sampled.[31] Therefore, HAADF imaging is also often referred to as Z-contrast imaging.

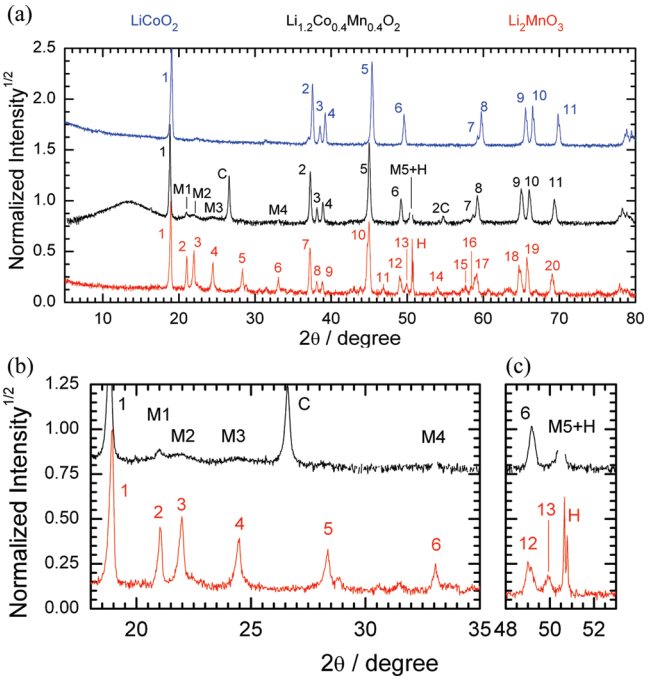


**Figure 2.** (a) XRD patterns from $Li_{1.2}Co_{0.4}Mn_{0.4}O_2$ (black), $Li_2MnO_3$ (red), and $LiCoO_2$ (blue) samples. The patterns are indexed with respect to $R\bar{3}m$ ($Li_{1.2}Co_{0.4}Mn_{0.4}O_2$ and $LiCoO_2$) and $C2/m$ ($Li_2MnO_3$) bases with lattice parameters indicated in Table 1. Additional peaks due to the carbonaceous binder (C and 2C), Li-ordering (weak peaks in the $20° \leq 2\theta \leq 26°$ range) and the sample holder (H) are present in the $Li_{1.2}Co_{0.4}Mn_{0.4}O_2$ and $Li_2MnO_3$ (H only) patterns. (b) $18° \leq 2\theta \leq 35°$ and (c) $48° \leq 2\theta \leq 53°$ regions of the $Li_{1.2}Co_{0.4}Mn_{0.4}O_2$ and $Li_2MnO_3$ patterns. The $Li_{1.2}Co_{0.4}Mn_{0.4}O_2$ pattern shows monoclinic reflections (M1−M5) that indicate Li ordering at the TM planes.

## 3. RESULTS AND DISCUSSION

**3.1. Secondary Electron Microscopy.** Figure 1 shows representative SEM images obtained on the $Li_{1.2}Co_{0.4}Mn_{0.4}O_2$-based electrode. Figure 1a shows the presence of the oxide, carbons (graphite, acetylene black), and the binder. The $Li_{1.2}Co_{0.4}Mn_{0.4}O_2$ secondary particles are ~10 $\mu$m in size and composed of an agglomerate of primary particles ~0.2−0.5 $\mu$m in size. Figure 1b shows the curved shapes of some primary particle boundaries; relatively clear facets can be seen within some of the primary particles (for example, those marked by black dotted lines).

**3.2. X-ray Diffraction.** Figure 2 shows three powder XRD patterns from $LiCoO_2$ (blue), $Li_2MnO_3$ (red), and $Li_{1.2}Co_{0.4}Mn_{0.4}O_2$ (black) samples, respectively. Overall, the spectra present relatively sharp peaks and high signal-to-noise ratios, indicative of the good crystalline quality of the samples. The patterns can be indexed with respect to appropriate unit cells (monoclinic for $Li_2MnO_3$ and rhombohedral for $LiCoO_2$ and $Li_{1.2}Co_{0.4}Mn_{0.4}O_2$), based on the reflections labeled with numerals on each spectrum. Table 1 lists the results of least-squares refinement of lattice parameters of each spectrum. Refinement residuals, peak assignments, observed and calculated peak positions, and overall $2\theta$ offsets are listed in the Supporting Information (see Tables S1, S2, and S3).

In addition to peaks arising from graphite and the sample holder (labeled C and H, respectively), a set of weak reflections labeled $M_i$, with $i = 1-5$, is also present in the $Li_{1.2}Co_{0.4}Mn_{0.4}O_2$ spectrum. These reflections cannot be indexed in terms of a


dx.doi.org/10.1021/cm200250a |Chem. Mater. 2011, 23, 2039–2050

**Table 1. Lattice Parameters Used To Index Powder XRD Patterns in Figure 1**[a]

| sample | rhombohedral lattice | monoclinic lattice |
|---|---|---|
| $LiCoO_2$ | $a$ = 2.8082 Å<br>$c$ = 14.0172 Å | |
| $Li_{1.2}Co_{0.4}Mn_{0.4}O_2$ | $a$ = 2.8260 Å<br>$c$ = 14.1454 Å<br>$a_{Vegard}$ = 2.826 (0%)<br>$c_{Vegard}$ = 14.129 (1.2%) | $a_M \equiv 3^{1/2}a$ = 4.8948 Å<br>$b_M \equiv 3a$ = 8.4780 Å<br>$c_M \equiv {}^1/_3(a_M{}^2 + c^2)^{1/2}$ = 4.9894 Å<br>$\beta_M \equiv \arcsin[c/(3c_M)]$ = 109.09° |
| $Li_2MnO_3$ | $a_{equiv}$ = 2.845 (±0.001, 0.04%)<br>$c_{equiv}$ = 14.2403 | $a$ = 4.9292 Å<br>$b$ = 8.5307 Å<br>$c$ = 5.0230 Å<br>$\beta$ = 109.09° |

[a] $LiCoO_2$ and $Li_{1.2}Co_{0.4}Mn_{0.4}O_2$ present a rhombohedral $R\bar{3}m$ structure, while $Li_2MnO_3$ presents a monoclinic $C2/m$ structure. An equivalent monoclinic unit cell, derived from the $R\bar{3}m$ structure, is presented for $Li_{1.2}Co_{0.4}Mn_{0.4}O_2$ to facilitate comparison to the $Li_2MnO_3$ lattice and to examine the origin of the Li-ordering peaks in terms of a monoclinic $Li_{TM}$ sublattice.

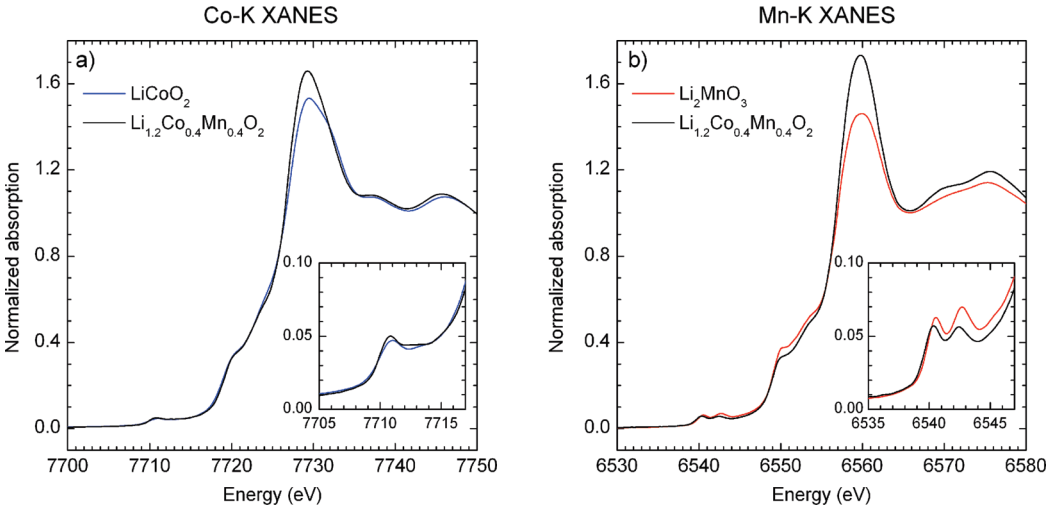


**Figure 3.** Normalized XANES spectra at the (a) Co K-edge and (b) Mn K-edge of $Li_{1.2}Co_{0.4}Mn_{0.4}O_2$ (black), $LiCoO_2$ (blue), and $Li_2MnO_3$ (red) samples. The inset in each figure contains a magnified view of the corresponding prepeak region.

rhombohedral structure, because of their absence in the $LiCoO_2$ spectrum, but they can be indexed in terms of a monoclinic superlattice, constructed from a unit cell derived from the rhombohedral reflections and consistent with Li ordering at the TM planes of the layered-rhombohedral $Li_{1.2}Co_{0.4}Mn_{0.4}O_2$ structure. The monoclinic lattice parameters are also included in Table 1, while the monoclinic indices of all $Li_{1.2}Co_{0.4}Mn_{0.4}O_2$ reflections are given in Table S2 in the Supporting Information.

**3.3. X-ray Absorption Spectroscopy.** Normalized Co and Mn K-edge XANES spectra for as-prepared $LiCo_{0.4}Mn_{0.4}O_2$ are shown in Figures 3a and 3b, respectively. Each spectrum is plotted together with a $LiCoO_2$ or $Li_2MnO_3$ standard for comparison; the prepeak area of each sample is shown in more detail in the corresponding inset. It is evident from Figures 3a and 3b that the energy position and edge shapes for as-prepared $LiCo_{0.4}Mn_{0.4}O_2$ are very similar to those from $LiCoO_2$ and $Li_2MnO_3$ standards, in which Co and Mn are in the +3 and +4 oxidation states, respectively.

Figure 4 shows Co K-edge and Mn K-edge EXAFS spectra recorded from a $Li_{1.2}Co_{0.4}Mn_{0.4}O_2$ sample (black lines); these spectra are compared with Co K-edge spectra from the $LiCoO_2$ sample (blue lines), and Mn K-edge spectra from the $Li_2MnO_3$ sample (red lines). Panels on the left of Figure 4 ((a), (c), and (e)) present Co K-edge spectra of the $Li_{1.2}Co_{0.4}Mn_{0.4}O_2$ sample and the $LiCoO_2$ standard, while panels on the right of Figure 4 ((b), (d), and (f)) present Mn K-edge spectra of the $Li_{1.2}Co_{0.4}Mn_{0.4}O_2$ sample and the $Li_2MnO_3$ standard. The top panels (Figures 4a and 4b) contain the ($k^3$-weighted) EXAFS $\chi(k)$ spectra, while the middle and bottom panels show its Fourier transform $F[\chi(R)]$; Figures 4c and 4d show the amplitude, and Figures 4e and 4f show the real part. The line color used for each spectrum is indicative of the originating sample, as explained above. Note that the Mn spectra are truncated at $k \simeq 11$ Å$^{-1}$, to avoid the overlap of any signal from Fe impurities.

It is evident that both Co and Mn EXAFS spectra from the $Li_{1.2}Co_{0.4}Mn_{0.4}O_2$ sample (black lines in Figures 4a and 4b, respectively) are remarkably similar to those of the corresponding $LiCoO_2$ and $Li_2MnO_3$ standards. The amplitude of the Co−$Li_{1.2}Co_{0.4}Mn_{0.4}O_2$ EXAFS spectrum is smaller than the


dx.doi.org/10.1021/cm200250a |Chem. Mater. 2011, 23, 2039–2050

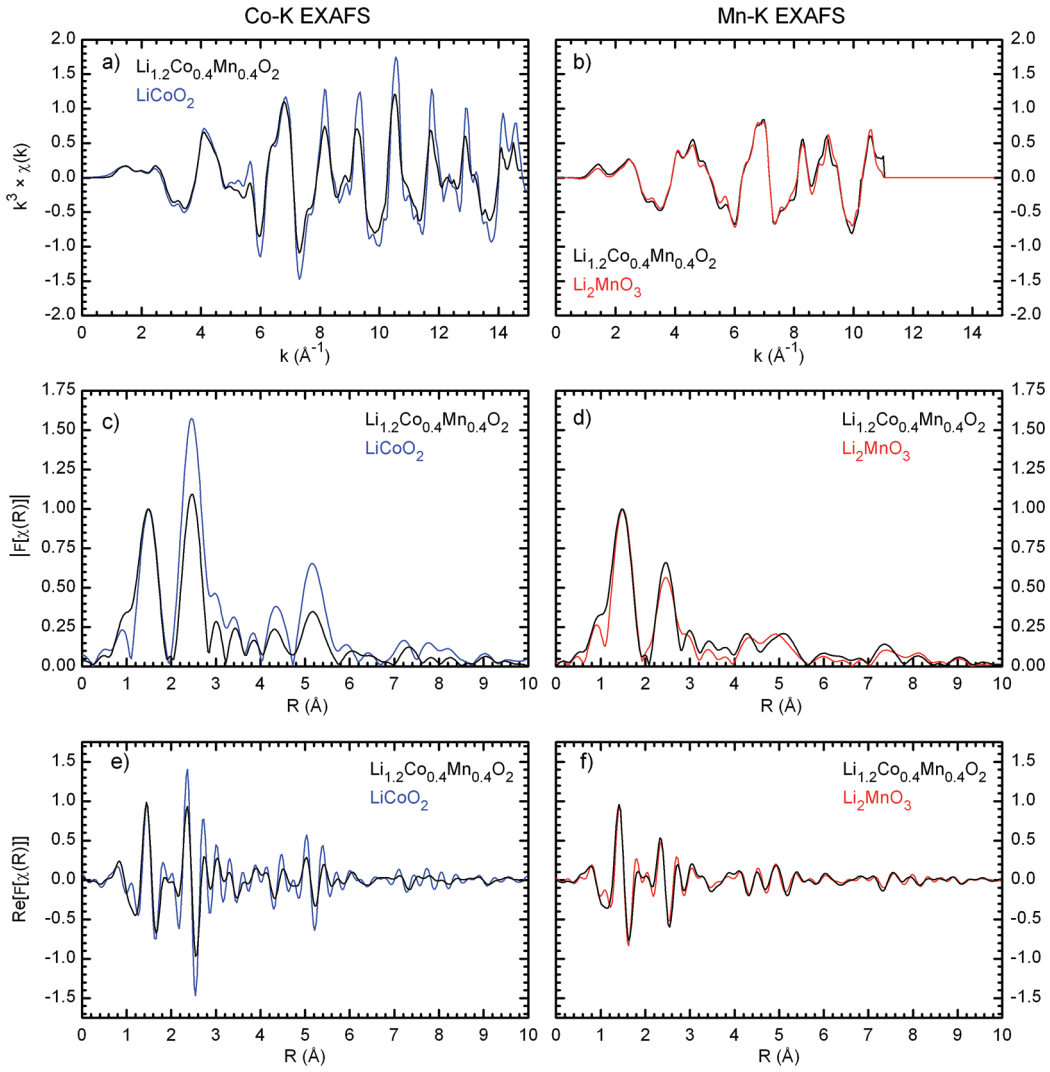


**Figure 4.** (a,b) $k^3$-weighted EXAFS spectra and (c−f) corresponding $k^3$-weighted Fourier transforms [(c,d) amplitude, (e,f) real part]. The spectra have been acquired at the (a,c,e) Co K-edge and (b,d,f) Mn K-edge of $Li_{1.2}Co_{0.4}Mn_{0.4}O_2$ (black), $LiCoO_2$ (blue), and $Li_2MnO_3$ (red) samples. Fourier-transformed spectra have been normalized to unit intensity at the first coordination shell.

Co-$LiCoO_2$ spectrum amplitude for $k \gtrsim 4$ Å$^{-1}$, suggesting a reduced coordination of higher-$Z$ elements (Mn, Co) to Co than in $LiCoO_2$. In contrast, the Mn- $Li_{1.2}Co_{0.4}Mn_{0.4}O_2$ EXAFS spectrum has similar amplitude to the Mn−$Li_2MnO_3$ spectrum throughout the entire $k$-range observed. These observations suggest that the local environments of Co and Mn absorbers in $Li_{1.2}Co_{0.4}Mn_{0.4}O_2$ are structurally similar to those in $LiCoO_2$ and $Li_2MnO_3$.

Structural information in EXAFS spectroscopy arises from interference of the photoelectron wave function with nearby atoms, which results in a modulation of the X-ray absorbance. Fourier transform (FT) spectra are commonly used to interpret, qualitatively, the structural information contained in the EXAFS spectrum, because different atomic shells contribute intensity to the FT-EXAFS at positions close to their distance from the absorber. However, note that the partial signals coming from different scattering shells are phase-shifted by different, element-specific amounts. Therefore, the effective scattering path distances, which are the abscissa of the FT-EXAFS plots, are approximately 0.3−0.4 Å shorter than the actual interatomic distances in the structure, and detailed modeling is required to extract accurate bond lengths from the spectrum.

Figures 4c and 4d present the modulus of the FT-EXAFS of $Li_{1.2}Co_{0.4}Mn_{0.4}O_2$, $LiCoO_2$, and $Li_2MnO_3$ at the Co and Mn edges. Both edges show pronounced peaks at $R \simeq 1.5$ Å, corresponding to scattering from the nearest-neighbor O-coordination shell (M−O), and at $R \simeq 2.4$ Å, mainly because of TM atoms (M) in the second coordination shell (M−M). Li atoms, although also present in the second coordination shell, are light scatterers and provide a negligible contribution to the EXAFS signal. In addition, a clear shoulder occurring at $R \simeq 3.0$ Å is present in the second EXAFS peak of both spectra, because of scattering from nearby O atoms in the third coordination shell about the metal absorber (M−O2). This shoulder is more pronounced at the Mn-edges, because of the smaller relative intensity of the Mn−M than the Co−M peak. Every spectrum in Figure 4 has been scaled to the intensity of the M−O FT-EXAFS peak to facilitate comparison. It can be readily seen that the Co−Co intensity of the $LiCoO_2$ standard (the blue line in Figure 4c) is ∼3 times larger than the corresponding Mn−Mn intensity of the $Li_2MnO_3$ standard (the red line in Figure 4d), because of the lower


dx.doi.org/10.1021/cm200250a |*Chem. Mater.* 2011, 23, 2039–2050

**Table 2. Parameters Obtained from Least-Squares Fits of Experimental EXAFS Spectra Acquired at the Co K-edge and the Mn K-Edge of the $LiCoO_2$, $Li_{1.2}Co_{0.4}Mn_{0.4}O_2$, and $Li_2MnO_3$ Samples**

| | Co K-Edge | | Mn K-Edge | |
|---|---|---|---|---|
| | $LiCoO_2$ | $Li_{1.2}Co_{0.4}Mn_{0.4}O_2$ | $Li_2MnO_3$ | $Li_{1.2}Co_{0.4}Mn_{0.4}O_2$ |
| $\chi_r^2$ | 96 | 46 | 252 | 169 |
| $S_0^2$ | 0.783 ± 0.075 | 0. 783 | 0.666 ± 0.110 | 0.666 |
| metal coordination | 6 | 5.30 ± 0.73 | 3 | 3.25 ± 1.07 |
| $\varepsilon_0$ | 0.655 ± 0.942 eV | 0.704 ± 0.741 eV | −0.10 ± 2.09 eV | 0.21 ± 1.85 eV |
| $\sigma^2$ | | | | |
| O1 | (3.12 ± 1.06) × $10^{-3}$ Å$^2$ | (3.24 ± 0.52) × $10^{-3}$ Å$^2$ | (1.23 ± 1.36) × $10^{-3}$ Å$^2$ | (1.89 ± 0.99) × $10^{-3}$ Å$^2$ |
| M | (2.04 ± 0.68) × $10^{-3}$ Å$^2$ | (3.42 ± 0.91) × $10^{-3}$ Å$^2$ | (2.92 ± 1.53) × $10^{-3}$ Å$^2$ | (1.92 ± 2.18) × $10^{-3}$ Å$^2$ |
| $R_{eff}$ | | | | |
| O1 | 1.916(7) Å | 1.916(5) Å | 1.904(10) Å | 1.905(10) Å |
| M | 2.823(5) Å | 2.834(3) Å | 2.853(13) Å | 2.855(6) Å |
| O2 | 3.402 Å | 3.411 Å | 3.511 Å | 3.486 Å |

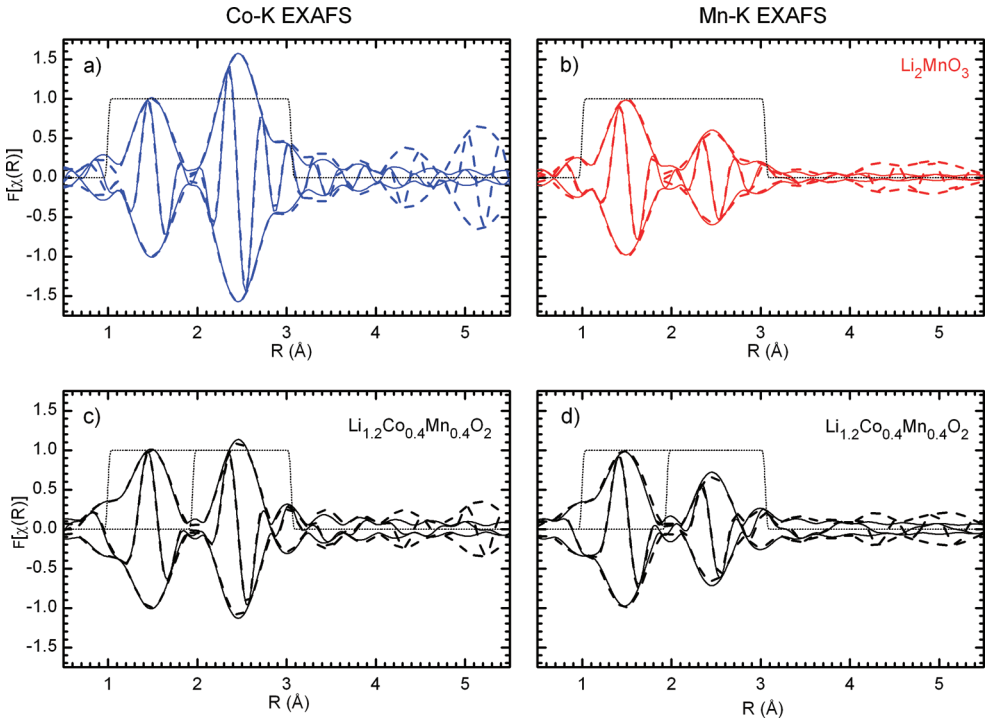


**Figure 5.** Least-squares fits of calculated FT-EXAFS phase and amplitude functions (continuous lines) to the experimental EXAFS spectra (dashed lines) shown in Figure 4. The spectra were acquired at (a, c) the Co K-edge and (b,d) the Mn K-edge of the $Li_{1.2}Co_{0.4}Mn_{0.4}O_2$ sample (black), the $LiCoO_2$ sample (blue), and the $Li_2MnO_3$ sample (red). Dotted lines delimit the fitting ranges being considered.

M−M coordination in the $Li_2MnO_3$ structure than in $LiCoO_2$ (3 and 6, respectively). Correspondingly, the $Li_{1.2}Co_{0.4}Mn_{0.4}O_2$ sample (black lines) shows ≃25% lower Co−M intensity than $LiCoO_2$ and ≃30% higher Mn−M intensity than $Li_2MnO_3$. These intensity differences are present throughout the entire spectra, with $Li_{1.2}Co_{0.4}Mn_{0.4}O_2$ generally showing lower intensity than $LiCoO_2$ at the Co edge and somewhat higher intensity than $Li_2MnO_3$ at the Mn edge, but keeping the same overall shape.

The same qualitative comparison can be made on the real part of the FT-EXAFS spectra (Figures 4e and 4f). Overall, the $Li_{1.2}Co_{0.4}Mn_{0.4}O_2$ spectra at the Co/Mn edges present a reduced/increased amplitude, with respect to the corresponding standards, but keep almost-perfect phase matching up to $R \simeq 7$ Å. The overall shape similarities and phase match of the $Li_{1.2}Co_{0.4}Mn_{0.4}O_2$ EXAFS spectra at Co and Mn edges to the standard spectra are indicative of the local atomic environments of Co and Mn being similar to that of $LiCoO_2$ and $Li_2MnO_3$, respectively; significant structural differences, if any, occur further than 3 or 4 nearest-neighbor distances away from the absorber. The EXAFS oscillation amplitude differences, with respect to the standards, indicate a small degree of light scatterer substitutionals (Li atoms or vacancies) at M-coordination shells about Co (diminished amplitude) and, correspondingly, heavy scatterer substitutionals (Co or Mn) at Li-sites in the Mn−M coordination shells (increased amplitude).


dx.doi.org/10.1021/cm200250a |*Chem. Mater.* 2011, 23, 2039–2050

The above qualitative observations can be confirmed by quantitative analysis of the EXAFS spectra to obtain structural parameters. This analysis is performed by least-squares fits of phase and amplitude functions, generated by the FEFF 6 code,[32] to the first two peaks of the Co and Mn FT-EXAFS. The calculated (continuous lines) and experimental (dashed lines) FT-EXAFS spectra are compared in Figures 5a−d. Both the real part and amplitude (plotted as the envelope of the real part) of the FT-EXAFS are presented at the Co edge (Figures 5a and 5c) and the Mn edge (Figures 5b and 5d) of $LiCoO_2$ (Figure 5a), $Li_2MnO_3$ (Figure 5b), and $Li_{1.2}Co_{0.4}Mn_{0.4}O_2$ (Figures 5c and 5d).

Table 2 summarizes the structural parameters resulting from the fitting procedure described in the Supporting Information; corresponding fits to the experimental data are given in Figure 5. In Table 2, the metal coordinations about Co and Mn in the $Li_{1.2}Co_{0.4}Mn_{0.4}O_2$ sample are 5.30 ± 0.73 and 3.25 ± 1.07, respectively. The corresponding coordination values for Co in $LiCoO_2$ and Mn in $Li_2MnO_3$ are 6 and 3, respectively. The expected coordination value for Co and Mn is 4.8 if these elements are randomly distributed in the TM plane of the $Li_{1.2}Co_{0.4}Mn_{0.4}O_2$ sample. For a structure where excess Li atoms occupy the (α) sites of a $\sqrt{3} \times \sqrt{3}$ sublattice in the TM planes, and Co and Mn occupy the remaining sites with equal probability, the coordination value for Co and Mn would be 4.5. Therefore, the Co−M coordination value in $Li_{1.2}Co_{0.4}Mn_{0.4}O_2$ is consistent with a structure model in which Co and Mn are randomly distributed in the TM plane, and a structure model in which Co and Mn segregate to form $LiCoO_2$-like and $Li_2MnO_3$-like areas. However, the Mn−M coordination value is closer to the latter structure model.

Furthermore, the $R_{eff}$ value for the Mn−M shell of $Li_{1.2}Co_{0.4}Mn_{0.4}O_2$ (2.855 ± 0.006 Å) is essentially identical to that of $Li_2MnO_3$ (2.853 ± 0.013 Å). The Co−M shell of $Li_{1.2}Co_{0.4}Mn_{0.4}O_2$ ($R_{eff}$ = 2.834 ± 0.003 Å) is somewhat larger than the Co−Co shell of $LiCoO_2$ ($R_{eff}$ = 2.823 ± 0.005 Å). Taken together, these observations suggest that excess Li at the TM planes of the $Li_{1.2}Co_{0.4}Mn_{0.4}O_2$ sample cluster preferentially around Mn atoms, resulting in a bimodal distribution of local chemical environments: $Li_2MnO_3$-like around Mn atoms and $LiCoO_2$-like around Co atoms. Deviations from the M−M coordination values expected for $LiCoO_2$ and $Li_2MnO_3$ can be attributed to boundary atoms shared by $LiCoO_2$- and $Li_2MnO_3$-like clusters. In addition, the coexistence of $LiCoO_2$- and $Li_2MnO_3$-like environments with different bond lengths (~1% mismatched) results in tensile strain on the $LiCoO_2$-like domains. This interpretation is consistent with the ~1.5× increase of the disorder parameter of the $Li_{1.2}Co_{0.4}Mn_{0.4}O_2$ Co−M shell [$\sigma^2$ = (3.42 ± 0.91) × $10^{-3}$ Å$^2$], with respect to the same shell in $LiCoO_2$ [$\sigma^2$ = (2.04 ± 0.68) × $10^{-3}$ Å$^2$], which is indicative of a more-disordered bonding environment. On the other hand, a structure model in which Co and Mn are randomly distributed in the TM planes would result in similar M−M shell radii, disorder parameters, and M−M coordination for the Co and Mn absorbers.

**3.4. Transmission Electron Microscopy.** Both X-ray techniques, XRD and XAS, provide sample information that constitutes an average over macroscopic sampling volumes. TEM analysis, on the other hand, allows the study of local variations in samples at nanometer scales. Simultaneous recording of real-space images by high-resolution electron microscopy (HREM) and HAADF-STEM, and of the reciprocal lattice by SAED, has been extensively applied to study the structure of Li-bearing oxides.[16−18,21,34−44]

In a recently published study,[28] we obtained SAED patterns, HAADF-STEM images, and EELS spectra from $Li_{1.2}Co_{0.4}Mn_{0.4}O_2$ samples to examine the local atomic structure and compared

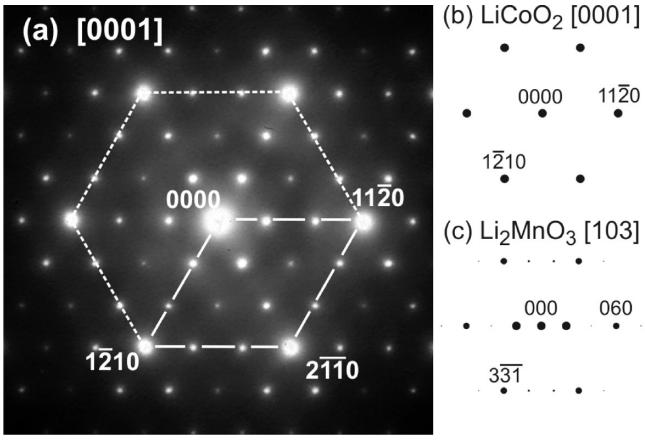


**Figure 6.** (a) [0001] SAED pattern of a $Li_{1.2}Co_{0.4}Mn_{0.4}O_2$ (primary) particle showing rhombohedral (fundamental) reflections and (monoclinic) 1/3 super-reflections along {11$\bar{2}$0}. (Reproduced with permission from ref 28. Copyright 2011, Elsevier.) (b, c) Simulated SAED patterns from equivalent zone axes in $LiCoO_2$ and $Li_2MnO_3$, obtained using WebEMAPS.[30]

the data with similar information from $Li_2MnO_3$ samples. In particular, we are interested in the possible segregation of $LiCoO_2$- and $Li_2MnO_3$-like domains in $Li_{1.2}Co_{0.4}Mn_{0.4}O_2$. In the following paragraphs, we summarize the main observations of our previous AEM study, in the interest of completeness and for the convenience of the reader. Later, we integrate these AEM results with the new data reported in this paper to propose a structural model, at the nanometer scale, of the integration of $Li_2MnO_3$ and $LiCoO_2$ blocks in the TM planes of $Li_{1+\alpha/3}Co_{1-\alpha}Mn_{2\alpha/3}O_2$, as a function of $LiCoO_2$ content. Only those results necessary to develop the proposed model are reproduced here, from ref 28, to which the reader is referred for full details of our AEM investigation.

SAED and HAADF-STEM present clear coexistence of $LiCoO_2$-like and $Li_2MnO_3$-like domains, while EELS shows relatively small (~10%) variation of the Co/Ni ratio in the TEM foil, down to thicknesses of 2−5 nm. The SAED carried out on individual grains of an ion-milled sample with selected-area apertures of 0.5 nm are exemplified in Figure 6a. The pattern exhibits strong rhombohedral reflections, indexed in four-index noatation, remisniscent of a $LiCoO_2$-like layered structure (see simulated pattern in Figure 6b). Superimposed onto the fundamental reflections are weaker 1/3 super-reflections that are associated with Li ordering in $Li_2MnO_3$-like domains. These super-reflections occur along three equivalent {11$\bar{2}$0} poles, rather than just one as would be expected in a single-crystal monoclinic $Li_2MnO_3$ sample (see the simulated pattern in Figure 6c). Therefore, the experimental pattern can be interpreted as the superposition of a rhombohedral $LiCoO_2$ pattern and three monoclinic $Li_2MnO_3$ patterns rotated 120° about the [0001] axis. Moreover, it can be understood as originating from coexisting rhombohedral ($LiCoO_2$-like) and monoclinic ($Li_2MnO_3$-like) structural domains as follows.

The monoclinic structure of $Li_2MnO_3$ and the rhombohedral structure of $LiCoO_2$ both consist of an alternating sequence of close-packed atomic planes, following a NaCl-like ABC stacking sequence with a Li-O-TM-O repeat motif. The basal TM plane of $Li_2MnO_3$ can be viewed as a $\sqrt{3} \times \sqrt{3} - R30°$ reconstruction of the $LiCoO_2$ basal TM plane, where Li atoms substitute for Mn at the sites of the $Li_{TM}$ reconstructed sublattice with Li atoms surrounded by six Mn neighbors in a $LiMn_6$ configuration and

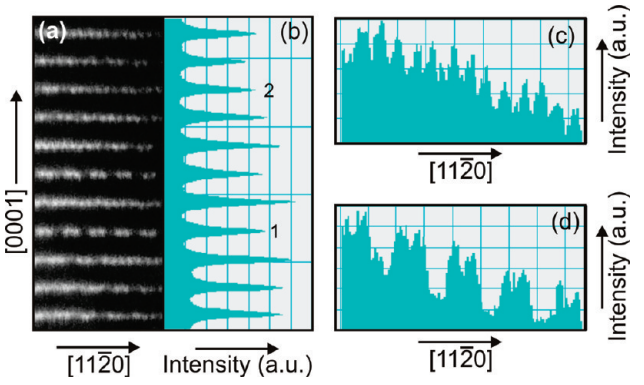


**Figure 7.** (a) HAADF image at the edge of a cleaved $Li_{1.2}Co_{0.4}Mn_{0.4}O_2$ grain along the [1$\bar{1}$00] zone axis. (b) Plot of HAADF intensity integrated along the corresponding rows in panel a. (c) HAADF intensity profile along the atomic row marked "2" in panel a. (d) HAADF intensity profile along the atomic row marked "1" in panel a. (All images in this figure have been reproduced with permission from ref 28. Copyright 2011, Elsevier.)

Mn atoms having three Li and three Mn neighbors. The monoclinic symmetry of $Li_2MnO_3$ stems from the relative alignment of $Li_{TM}$ sublattices across consecutive TM planes in the stack. As a consequence, and neglecting small lattice constant variations that can be accommodated by lattice strain in actual samples, $Li_2MnO_3$ shows a high structural compatibility with $LiCoO_2$ and both structures can, in principle, coexist together, sharing a common fcc-O lattice. In this context, there are three possible relative orientations (topotaxial relations) of the $Li_2MnO_3$ and $LiCoO_2$ structures: these are the 120° rotations of $[001]_M$ about the $[0001]_R$ axis. All three orientations share the TM plane of both $Li_2MnO_3$ and $LiCoO_2$, but the $Li_2MnO_3$ *c*-axis (the $Li_{TM}$ alignment direction across consecutive TM planes) can assume any of three possible orientations, viz, parallel to the [$\bar{1}$101], [0$\bar{1}$11] or [10$\bar{1}$1] directions in $LiCoO_2$, the orientations of which differ from each other just by a 120° rotation about the [0001] axis.

Within individual TM planes, hexagons of $LiMn_6$ and $Co_7$ coexist as building blocks of $Li_2MnO_3$ and $LiCoO_2$. These are best-imaged in Z-contrast with the TM planes viewed edge-on, in the direction perpendicular to the bonds. In such a projection, atomic columns in $LiMn_6$ domains follow a succession of pure Li and two pure Mn columns, which result in an alternating sequence of two high-brightness spots and one dark spot in HAADF-STEM images, with a periodicity of 0.42 nm (= 3 × 1.4 nm). Correspondingly, $LiCoO_2$ domains consist only of pure Co columns, which appear as high-brightness columns with 0.14 nm separation in HAADF-STEM images. Figure 7 exemplifies the HAADF-STEM observations obtained in this fashion; further experimental images can be found in Figure S2 in the Supporting Information.

Figure 7a presents a [1$\bar{1}$00] micrograph of a thin region (a few nanometers thick) at the edge of a cleaved grain in a $Li_{1.2}Mn_{0.4}Co_{0.4}O_2$ crushed powder sample. The thickness of the specimen increases from right to left in the micrograph, resulting in increasing average intensity. A clear $Li_2MnO_3$-like dot contrast is seen along some of the projected (0001) planes, while some (0001) planes show $LiCoO_2$-like continuous contrast.

Figure 7b shows the integrated intensity along the entire rows of Figure 7a. It can be seen that TM planes showing a pronounced dot contrast (e.g., the row marked "1" in Figure 7a) present a somewhat reduced integrated intensity, with respect to neighboring planes, suggesting a lower TM content.

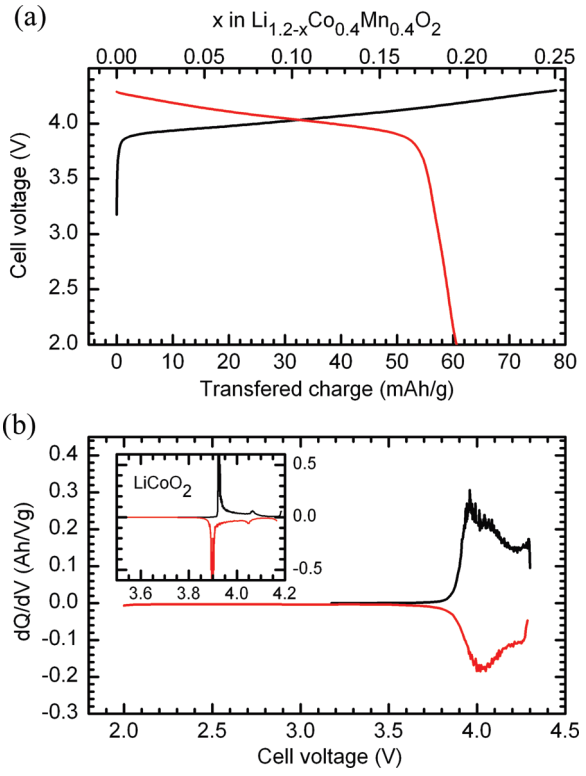


**Figure 8.** First-cycle (a) capacity−voltage and (b) d*Q*/d*V* plots, obtained from a $Li_{1.2}Co_{0.4}Mn_{0.4}O_2$//Li cell. The inset in panel b is a d*Q*/d*V* curve from a $LiCoO_2$//Li cell.

Figures 7c and 7d respectively show HAADF intensity profiles along the projected TM panes marked "2" and "1" in Figure 7a. The bright-bright-dark pattern along row 1 is clearly visible in the intensity profile in Figure 7d, where every third period in the intensity modulation is suppressed, although the separation between two consecutive bright dots is not nearly as pronounced as the intensity dip between two consecutive pairs of bright dots. The intensity profile in Figure 7c, corresponding to row 2 in Figure 7a, presents a periodic intensity modulation where each atomic column is clearly resolved.

EELS spectra were acquired in STEM mode, using a 1−1.5 Å wide electron probe, on several [1$\bar{1}$00]-oriented grains from both ion-milled and crushed-powder samples. In order to minimize beam damage, EELS scans were recorded taking care to confine the beam path to a region of the sample presenting either clear dotted $Li_2MnO_3$-like or continuous $LiCoO_2$-like contrast, similar to that presented in Figure 7. Comparison of the area under Co $L_{23}$ peaks (for details, see ref 28) in both spectra suggests that the Co/Mn atomic concentration ratio is ≳10% larger at regions of the image displaying continuous contrast. This value is a lower estimate of the actual composition difference between $Li_2MnO_3$-like and $LiCoO_2$-like contrast regions in sample thicknesses in the range of 2−5 nm.

**3.4. Electrochemistry.** Figure 8 shows the electrochemical profile, and the corresponding differential capacity (d*Q*/d*V* vs *V*) plot of a $Li_{1.2}Co_{0.4}Mn_{0.4}O_2$//Li cell during its first charge−discharge cycle between 4.3 V and 2 V with a current of 5.4 mA/g. The charge curve shows a rapid initial voltage rise to ∼3.9 V, after which the cell voltage continues to increase

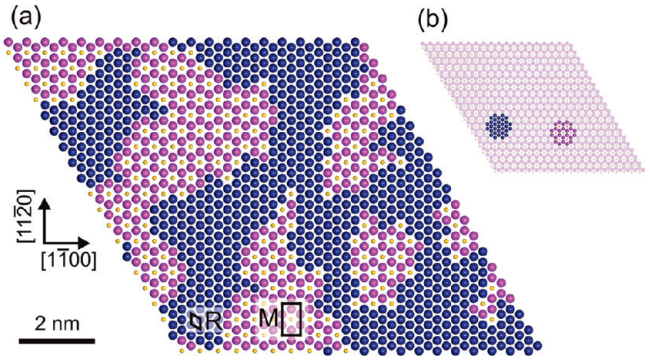


**Figure 9.** (a) Schematic model structure of a TM plane in $Li_{1.2}Co_{0.4}Mn_{0.4}O_2$, showing coexistence of Co and $LiMn_2$ domains. Large blue and magenta spheres represent Co and Mn atoms, respectively; small yellow spheres represent Li atoms. In-plane sections of the rhombohedral (R) and monoclinic (M) unit cells are indicated in the figure. Periodic boundary conditions connect the top and left edges of the figure with the bottom and right edges, respectively. Therefore, the particular model shown contains only one Co and two $LiMn_2$ separate clusters. In addition, projected atomic columns along $\langle 1\bar{1}00\rangle$ (e.g., left to right) contain approximately equal amounts of Co and X atoms, where X varies across columns following a Mn−Mn−Li sequence consistent with STEM results. (b) Illustration of the early stages of model generation showing one $LiMn_2$ and one Co cluster randomly placed on the board. Empty sites are indicated by faded colors.

monotonically at a much slower rate; the corresponding d$Q$/d$V$ plot shows a relatively sharp peak near 3.9 V. A similar sharp peak at 3.9 V is also visible in the $LiCoO_2$ d$Q$/d$V$ spectrum (see inset of Figure 8b); this 3.9 V peak corresponds to the insulator-to-metal transition of $LiCoO_2$, which has been reported to result in a biphasic region. Therefore, the ∼3.9 V peak in the $Li_{1.2}Co_{0.4}Mn_{0.4}O_2$ d$Q$/d$V$ plot indicates that the sample has considerable $LiCoO_2$-like character.

While examining the electrochemical and thermal behavior of $LiCo_{1-z}[MnMg]_{z/2}O_2$ samples, Luo et al.[45] noted that even small additions of Mg and Mn ($z = 0.1$) to $LiCoO_2$ reduce the intensity of the 3.9 V peak in d$Q$/d$V$ plots; the peak was nonexistent at $z \geq 0.2$ (i.e., when more than 20% of the Co is replaced by Mg and Mn). A similar observation was reported by Zeng et al.,[46] who doped $LiCoO_2$ with Ni and Mn to generate a series of $Li[Ni_xMn_xCo_{(1-2x)}]O_2$ samples. The 3.9 V peak in the d$Q$/d$V$ plots gradually broadened as $x$ increased from 0.02 to 0.15, and then disappeared for $x \geq 0.2$. That is, the $LiCoO_2$-like character in $Li[Ni_xMn_xCo_{(1-2x)}]O_2$ samples disappeared when more than 20% of the Co was replaced by Ni and Mn. This disappearance was correlated to the gradual loss of intensity observed in NMR spectra at resonances resulting from the presence of $Li(Co_6)^{first}(Co_6)^{second}$ local environments. The change in lithium-ion deintercalation mechanisms for $x \geq 0.2$ was ascribed to the disappearance of isolated $Co^{3+}$ clusters.[46]

In contrast, therefore, is the relatively sharp 3.9 V d$Q$/d$V$ peak in the $Li_{1.2}Co_{0.4}Mn_{0.4}O_2$ (= $Li[Li_{0.2}Co_{0.4}Mn_{0.4}]O_2$) samples, in which 60% of the Co is replaced by Li and Mn. Taken together with the NMR data reported by Zeng and co-workers,[46] our data indicate that the $LiCoO_2$-like areas within $Li_{1.2}Co_{0.4}Mn_{0.4}O_2$ extend over at least 2 to 3 coordination shells (i.e., a radius of ∼4 Å from the central Co atom).

The intensities in the $Li_{1.2}Co_{0.4}Mn_{0.4}O_2$ d$Q$/d$V$ plot between 3.9 and 4.2 V are likely associated with a series of lattice arrays, having distinguishably characteristic Gibbs energies, that are formed in the oxides as the Li lattice occupancy fraction progressively decreases during oxide delithiation. During cell discharge from 4.3 V to 2 V, the cell capacity was only 60 mAh/g, which is lower than the 80 mAh/g charge capacity obtained for the same voltage window; this capacity difference, which was not observed during subsequent cycles, may be partially attributed to kinetic factors that limit the oxide's ability to intercalate $Li^+$ at the currents used for cycling.[47] The discharge cycle d$Q$/d$V$ plot is similar to that for the charge cycle, allowing for the capacity loss and polarization effects associated with the cell's nonzero impedance.

**3.5. Structure of TM Planes.** Evidence for the existence of distinct $Li_2MnO_3$ and $LiCoO_2$ building blocks in the as-prepared $Li_{1.2}Co_{0.4}Mn_{0.4}O_2$ sample can be summarized as follows. The electrochemical behavior of $Li_{1.2}Co_{0.4}Mn_{0.4}O_2$ under initial charge suggests significant $LiCoO_2$-like character, while the XAS data indicate that a majority of TM atoms consist of $Co^{3+}$ and $Mn^{4+}$ in $LiCoO_2$ and $Li_2MnO_3$ chemical environments, extending at least 6−7 Å away from the corresponding TM atom; i.e., over the spatial sensitivity range of the EXAFS probe. XRD data reveal an overall layered rock salt (rhombohedral) framework with trace monoclinic reflections. SAED, which is much more sensitive to local arrangements, because of the smaller coherence length of the electron probe, reveals $Li_{TM}$ ordering in a monoclinic sublattice that locally exists in either of three orientations (120° rotations of $[001]_M$ about the $[0001]_R$ axis), coherent with the overall rhombohedral framework. HAADF-STEM images display two different types of contrast along TM-rich planes, dotted and continuous, respectively consistent with locally monoclinic ($Li_2MnO_3$-like) or rhombohedral ($LiCoO_2$-like) structures. However, EELS examination did not reveal significant composition differences between both types of areas. These observations suggest an overall rhombohedral structure in which TM planes Co and $LiMn_2$ building blocks are integrated and share common O and Li planes, as has been previously proposed.[16,27]

In the following paragraphs, we focus on understanding the distribution of Co, Mn, and Li on a TM-rich plane. Our goal is to map, as a function of composition, the geometries that (1) result from combining Co and $LiMn_2$ clusters with a minimum size greater than ∼7 Å, consistent with our EXAFS results indicating $LiCoO_2$- and $Li_2MnO_3$-like near-atomic environments about Co and Mn, respectively; (2) are consistent with a homogeneous Co−Mn distribution at a probing scale of a few nanometers, as suggested by our EELS results; and (3) result in projected structures consistent with experimental HAADF-STEM images. Rather than attempting full-fledged *ab initio* or molecular dynamics (MD) modeling of $Li_{1.2}Co_{0.4}Mn_{0.4}O_2$, which falls beyond the scope of the present work, we employ a stochastic algorithm to generate model TM-plane structures (Figure 9a) corresponding to possible microstates present in the ensemble of a $Li_{1+x/3}Co_{1-x}Mn_{2x/3}O_2$ sample. By choosing a suitable minimum cluster size, common to $LiMn_2$ and Co clusters, these model microstates are constrained by construction to be consistent with our EXAFS results.

Our modeling process starts with a two-dimensional board containing a hexagonal lattice of empty sites (faded-colored spheres in Figure 9b) on which periodic boundary conditions are imposed. This board is congruent with the $\sqrt{3} \times \sqrt{3}$ −$R30°$ $Li_{TM}$ sublattice, with sides running parallel to $\langle 0\bar{1}10\rangle$ directions in the hexagonal plane. The board length ($s$) is defined as the number of second nearest-neighbor spacings (i.e., $Li_{TM}$−$Li_{TM}$ ≈ 4.9 Å in $Li_2MnO_3$) along its side. In order to generate a model structure of size $s$ and composition $p$ $Li_2MnO_3 \cdot (1 - p)$ $LiCoO_2$, the board is populated according to the following algorithm.


dx.doi.org/10.1021/cm200250a |*Chem. Mater.* 2011, 23, 2039–2050

First, an empty board site is randomly selected, which becomes the center of the 21-atom cluster to be filled. Then, a cluster type, either $Li_2MnO_3$ or $LiCoO_2$, is chosen with probability $p$ determined by the intended model composition. For a $Li_2MnO_3$ cluster type, Li atoms are placed at the cluster center, as well as its six second-nearest neighbors; and the 14 remaining cluster sites, all of them nearest-neighbors to Li, are filled with Mn. For a $LiCoO_2$ cluster type, all 21 sites in the cluster are filled with Co. Figure 9b presents an example of the earlier stages of model generation containing two clusters: one Co and one $LiMn_2$.

The above process is iterated until the entire board is filled. As the board is populated, the probability that the new cluster would overlap already populated sites increases. If the new cluster, centered at a randomly selected empty site, overlaps filled sites of equal type, the cluster type is not selected randomly, but the existing region is expanded to fill the new cluster.

Figure 9a presents a typical model structure of a $Li_{1.2}Co_{0.4}Mn_{0.4}O_2$ TM-plane generated using the above algorithm. In particular, the board side is $s = 20$ $Li_{TM}-Li_{TM}$ spacings long (~10 nm), and the target composition is $p = 0.5$. The actual model composition corresponds to 0.454 ($Li_{2.006}Mn_{0.994}O_3$) + 0.546 ($LiCoO_2$), after introducing appropriate Li and O planes. The overall geometrical features of the model are consistent with experimental results, although no configuration energies were considered in generating the model. In particular, most of the metal atoms in the model experience an end-member-like atomic environment up to, at least, two or three in-plane nearest neighbors (~5 and 6 Å, respectively). In addition, when this plane is projected edge-on (e.g., from left to right in the figure), its $\langle 1\bar{1}00\rangle$-projected columns contain ~50% Co and ~50% Mn or Li.

The particular model structure shown in Figure 9a contains two separate $Li_2MnO_3$ regions and one continuously connected $LiCoO_2$ region. Our algorithm does not consider misaligned $Li_2MnO_3$ regions. Nevertheless, the relative alignment of different $Li_2MnO_3$ domains overlapping within the sample depth is responsible for the observed continuous or discontinuous HAADF-STEM contrast, which is proportional to the atomic mass of the projected atomic columns.

Figures 10a and 10b contain two schematics of possible arrangements of coexisting $LiCoO_2$-like and $Li_2MnO_3$-like domains in a TM(0001) plane. Moreover, Figures 10c and 10d show the corresponding atomic mass variation (arbitrary units, assuming $Z_{Li} \ll Z_{Co} \approx Z_{Mn}$) of $[0\bar{1}10]$ atomic columns (the vertical direction in the schematics) along the $[2\bar{1}\bar{1}0]$ axis (the horizontal direction in schematics). The schematic in Figure 10a shows an area of a TM(0001) plane containing one $LiCoO_2$-like cluster (bottom half), where every TM site is occupied by Co atoms (blue dots), and one $Li_2MnO_3$-like cluster (top half), where each Li atom (yellow dots) is surrounded by six Mn atoms (magenta dots). The schematic in Figure 10b shows two $Li_2MnO_3$-like clusters separated by a $LiCoO_2$-like cluster. The two $Li_2MnO_3$-like clusters in Figure 10b are misaligned, with Li$[0\bar{1}10]$ columns in the bottom cluster overlapping with Mn columns in the upper cluster. In other words, the schematic structure in Figure 10b corresponds to an $Li_2MnO_3$ antiphase boundary[16] in the TM plane, decorated by Co.

Both configurations result in a projected $Z$ oscillation along $[2\bar{1}\bar{1}0]$ with a periodicity of $1.5 \times a_h$ ($\approx$ 4.24 Å, where $a_h$ is the nearest-neighbor distance of the TM plane) that is due to the superposition of Mn-rich columns onto a continuous background due to Co. The projected $Z$ profile shown in Figure 10c (corresponding to Figure 10a) contains peaks that are twice as wide as the valleys separating them, because of the occurrence of two Li-free columns in the sequence. In contrast, the valleys in Figure 10d (corresponding to Figure 10b) are twice as wide as the peaks, because of the occurrence of two consecutive Li-containing columns. The intensity in the valleys of Figure 10c is entirely due to Co, because no Mn is present in these columns, and is expected to result in a HAADF-STEM profile similar to a TM plane in $Li_2MnO_3$, albeit with reduced bright-to-dark columns contrast, because of the Co present in the low-$Z$ (Mn-free) columns.[18,39] However, the valleys in Figure 10d correspond to columns containing both Co, as well as Mn and Li; while the peaks correspond to Li-free columns, as in Figure 10c. In addition, the resulting HAADF-STEM contrast is expected to resemble a continuous stripe, perhaps with a faint modulation due to the presence of heavier Li-free columns.

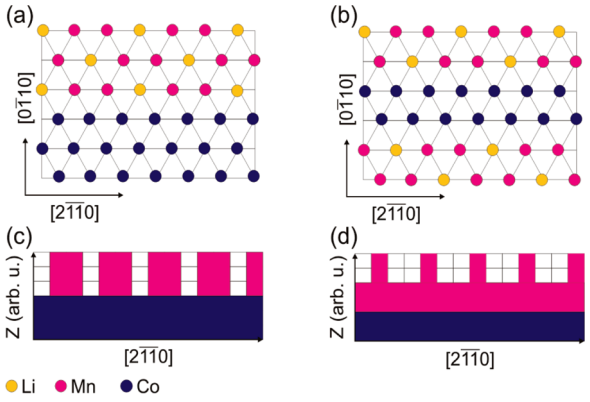


**Figure 10.** (a, b) Schematics of two possible configurations of a $Li_{1.2}Co_{0.4}Mn_{0.4}O_2$ TM plane in a thin STEM sample. (c, d) Corresponding plots of the projected atomic mass of $[0\bar{1}10]$ columns (the vertical direction in the schematics).

Lacking long-range interactions between disconnect $Li_2MnO_3$ regions or interconnection through neighboring TM planes in the layered rock salt sequence, the probability of two $Li_2MnO_3$ regions being aligned is $p_A(2) = 1/3$. Consequently, the probability that N $Li_2MnO_3$ regions are all aligned is $p_A(N) = 3^{1-N}$. Therefore, statistics on the number of separate $Li_2MnO_3$ regions in the model TM planes, as a function of model size and composition, can be taken as proxy for the probability of observing dotted ($Li_2MnO_3$-like) or continuous ($LiCoO_2$-like) HAADF-STEM contrast in comparable samples.

Figure 11a presents plots of the number of separate clusters ($LiMn_2$ on the left axis and Co on the right axis) as a function of composition, for model sizes $s$ = 11, 18, and 25. The curves interpolating the data points are meant only to guide the reader's eye. Representative TM microstructures are given in Figures 11b, 11c, 11d, and 11e, which are sections of different models generated with $s$ = 45 and $p$ = 0.15, 0.45, 0.75, and 0.90, respectively.

Not surprisingly, close to the end-member composition, the models are homogeneous, consisting only of one cluster of the major component. This is reflected in the fast drop in the number of Co clusters (blue symbols, right axis) close to $Li_2MnO_3$ composition ($x = 1$) and its leveling to a value of one cluster for compositions close to $LiCoO_2$ ($x = 0$). Conversely, the number of $LiMn_2$ clusters (black symbols, left axis) shows a similar tendency at opposite ends of the composition axis. Models with small sizes ($s \lesssim 13$) consist essentially of a single Co and a single $LiMn_2$ cluster, with their relative sizes dictating the model composition ($x$).

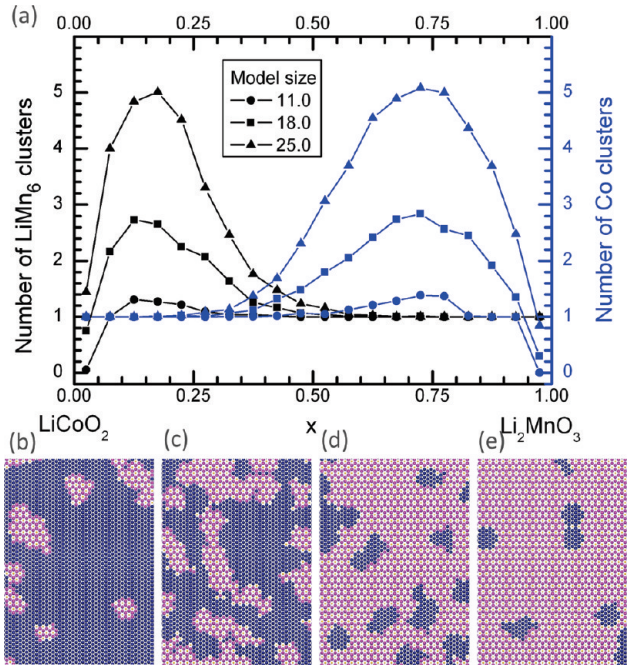


**Figure 11.** (a) Number of disconnect clusters ($LiMn_2$ on left axis, Co on right axis), as a function of composition for three model sizes ($s$ = 11, 18, and 25). (b−e) Sections of large model TM planes ($s$ = 45) with target compositions (b) $p$ = 0.15, (c) $p$ = 0.45, (d) $p$ = 0.75, and (e) $p$ = 0.90, illustrating the expected morphology evolution from small isolated clusters of the minority constituent at both ends of the composition range to large, noncompact, well-integrated domains of both constituents toward the middle of the composition range.

Moreover, a large model size ($s$ > 15) is necessary to allow a small cluster of the minority component without deviating significantly from the end-member composition. (See Figure S4 in the Supporting Information.) In this case, typical configurations contain several compact clusters of the minor component dispersed in a matrix of the major component. For example, Figure 11b shows a TM plane configuration containing a set of $LiMn_2$ clusters well-dispersed in a Co matrix, while Figure 11e shows the complementary case close to $Li_2MnO_3$ composition.

Compositions close to $x \approx 0.5$ (like the sample studied above) contain essentially one cluster of each component. This time, the clusters are not compact but dendritic (see Figures 9a and 11c), allowing for a single connected cluster to extend over long ranges in the plane. Therefore, the complex, interpenetrating geometry of these clusters explains all of the experimental observations described above:

(1) Over length scales below 1 nm, most, if not all, neighbors to any given atom belong to the same cluster type, as observed by EXAFS; with small deviations from the end-member M−M correlation values due to atoms sitting at the dendrite boundaries.

(2) Approximately equal amounts of Co and Mn are present over length scales between 1 nm and a few nanometers, because of the presence of both $LiMn_2$ and Co clusters; which is consistent with EELS observations where lateral delocalization and sample thickness limit the resolution to these levels.[28]

(3) Because only one $LiMn_2$ cluster is expected over distances of $s$ = 25 (∼12 nm), in-plane Li-ordering coherence is maintained over long distances; which is consistent with the HAADF-STEM observation of $Li_2MnO_3$-like dotted contrast on TM(0001) rows over distances significantly longer length scale probed by EXAFS.

## 4. CONCLUSIONS

We employed a combination of SEM, XRD, EXAFS, and AEM analyses to examine the structure of as-prepared $Li_{1.2}Co_{0.4}Mn_{0.4}O_2$ at atomic and nanometer scales. SEM and XRD revealed that the sample possesses an overall $R\bar{3}m$ structure similar to $LiCoO_2$, and that primary particles ∼0.2−0.5 $\mu$m in size agglomerate to form bigger (∼7 $\mu$m) secondary particles. SAED revealed the coexistence of monoclinic $Li_2MnO_3$-like and rhombohedral $LiCoO_2$-like crystal structures, consistent with the HAADF-STEM observation of Li-ordering at TM planes of the host rhombohedral lattice. EXAFS revealed distinct segregation of Mn and Co into almost undistorted $LiCoO_2$-like and $Li_2MnO_3$-like atomic environments over length scales of at least 7 Å. In contrast, EELS analyses revealed coexistence of Co and Mn, in roughly equal proportions, over length scales of <1 nm. This apparent contradiction is resolved by a proposed model consisting of well-integrated $LiCoO_2$ and $Li_2MnO_3$ nanoclusters which, for compositions close to 0.5 $Li_2MnO_3$·0.5 $LiCoO_2$ = $Li_{1.2}Co_{0.4}Mn_{0.4}O_2$ presents a microstructure composed of well-integrated dendritic clusters. The small width of the dendrites (∼1 nm) accounts for both the almost-perfect segregation into $LiCoO_2$ and $Li_2MnO_3$ at EXAFS scales and the almost-homogeneous concentrations of Mn and Co at EELS scales. The dendritic nature of the clusters, allowing them to retain continuity over long distances in the TM(0001) plane, accounts for the large lateral extension of the $Li_2MnO_3$-like contrast regions observed in HAADF-STEM. Because no specific atomic interactions were used in obtaining the atomistic models, we expect the proposed microstructures to be valid for other Li-$(Li_xTM_yMn_{1-x-y})O_2$ materials that display Li-ordering within the TM(0001) planes of a host rhombohedral structure.

## ■ ASSOCIATED CONTENT

**Supporting Information.** This material is available free of charge via the Internet at http://pubs.acs.org.

## ■ AUTHOR INFORMATION

### Corresponding Author

*Tel.: 630 252 0593 (M.B.), 630 252 4332 (D.P.A.). E-mail addresses: mali@aps.anl.gov (M.B.), abraham@anl.gov (D.P.A.).

### Notes

†The submitted manuscript has been created by UChicago Argonne, LLC, Operator of Argonne National Laboratory ("Argonne"). Argonne, a U.S. Department of Energy Office of Science laboratory, is operated under Contract No. DE-AC02-06CH11357. The U.S. Government retains for itself, and others acting on its behalf, a paid-up nonexclusive, irrevocable worldwide license in said article to reproduce, prepare derivative works, distribute copies to the public, and perform publicly and display publicly, by or on behalf of the Government.

## ■ ACKNOWLEDGMENT

Support from the U.S. Department of Energy's Vehicle Technologies Program, and specifically from Dave Howell, is gratefully acknowledged. The submitted manuscript has been created by UChicago Argonne, LLC, Operator of Argonne National Laboratory ("Argonne"). Argonne, a U.S. Department of Energy Office of Science laboratory, is operated under Contract No. DE-AC02-06CH11357. PNC/XSD facilities at the Advanced Photon Source, and research at these facilities, are supported by the U.S. Department of Energy—Basic Energy Sciences, a Major Resources Support grant from NSERC, University of Washington, Simon Fraser University, and the Advanced Photon Source. Use of the Advanced Photon Source is also supported by the U.S. Department of Energy, Office of Science, Office of Basic Energy Sciences, under Contract DE-AC02-06CH11357. We acknowledge use of the Center for Microanalysis of Materials (CMM) at the Frederick Seitz Materials Research Laboratory, University of Illinois at Urbana—Champaign (Illinois), which is partially supported by the U.S. Department of Energy (under Grant Nos. DE-FG02-07ER46453 and DE-FG02-07ER46471).

## ■ REFERENCES

(1) Mikkelsen, J. C., Jr.; Boyce, J. B. *Phys. Rev. B* **1983**, *28*, 7130.
(2) Boyce, J. B.; Mikkelsen, J. C., Jr. *Phys. Rev. B* **1985**, *31*, 6903.
(3) Frenkel, A.; Stern, E. A.; Voronel, A.; Qian, M.; Newville, M. *Phys. Rev. Let.* **1993**, *71*, 3485.
(4) Sakamoto, K.; Hirayama, M.; Sonoyama, N.; Mori, D.; Yamada, A.; Tamura, K.; Mizuki, J.; Kanno, R.. *Chem. Mater.* **2009**, *21*, 2632.
(5) Marichal, C.; Hirschinger, J.; Granger, P.; Ménétrier, M.; Rougier, A.; Delmas, C. *Inorg. Chem.* **1995**, *34*, 1773.
(6) Rougier, A.; Saadoune, I.; Gravereau, P.; Willmann, P.; Delmas, C. *Solid State Ionics* **1996**, *90*, 83.
(7) Nakai, I.; Takahashi, K.; Shiraishi, Y.; Nakagome, T.; Izumi, F.; Ishii, Y.; Nishikawa, F.; Konishi, T. *J. Power Sources* **1997**, *68*, 536.
(8) Ohzuku, T.; Ueda, A.; Nagayama, M. *J. Electrochem. Soc.* **1993**, *140*, 1862.
(9) Peres, J. P.; Demourgues, A.; Delmas, C. *Solid State Ionics* **1998**, *111*, 135.
(10) Balasubramanian, M.; Sun, X.; Yang, X. Q.; McBreen, J. *J. Power Sources* **2001**, *92*, 1.
(11) Balasubramanian, M.; Sun, X.; Yang, X. Q.; McBreen, J. *J. Electrochem. Soc.* **2000**, *147*, 2903.
(12) Mansour, A. N.; Yang, X. Q.; Sun, X.; McBreen, J.; Croguennec, L.; Delmas, C. *J. Electrochem. Soc.* **2000**, *147*, 2104.
(13) Chung, J.-H.; Proffen, Th.; Shamoto, S.; Ghorayeb, A. M.; Croguennec, L.; Tian, W.; Sales, B. C.; Jin, R.; Mandrus, D.; Egami, T. *Phys. Rev. B* **2005**, *71*, 064410.
(14) Van der Ven, A.; Aydinol, M. K.; Ceder, G.; Kresse, G.; Hafner, J. *Phys. Rev. B* **1998**, *58*, 2975.
(15) Arroyo y de Dompablo, M. E.; Van der Ven, A.; Ceder, G. *Phys. Rev. B* **2002**, *66*, 064112.
(16) Meng, Y. S.; Ceder, G.; Grey, C. P.; Yoon, W.-S.; Jiang, M.; Bréger, J.; Shao-Horn, Y. *Chem. Mater.* **2005**, *17*, 2386.
(17) Croguennec, L.; Shao-Horn, Y.; Gloter, A.; Colliex, C.; Guilmard, M.; Fauth, F.; Delmas, C. *Chem. Mater.* **2009**, *21*, 1051.
(18) Lei, C. H.; Wen, J. G.; Sardela, M.; Bareño, J.; Petrov, I.; Kang, S.-H.; Abraham, D. P. *J. Mater. Sci.* **2009**, *44*, 5579.
(19) Massarotti, V.; Bini, M.; Capsoni, D.; Altomare, A.; Moliterni, A. G. G. *J. Appl. Crystallogr.* **1997**, *30*, 123.
(20) Strobel, P.; Lambert-Andron, B. *J. Solid State Chem.* **1998**, *75*, 90.
(21) Boulineau, A.; Croguennec, L.; Delmas, C.; Weill, F. *Chem. Mater.* **2009**, *21*, 4216.
(22) Bréger, J.; Kang, K.; Cabana, J.; Ceder, G.; Grey, C. P. *J. Mater. Chem.* **2007**, *17*, 3167.
(23) Balasubramanian, M.; McBreen, J.; Davidson, I. J.; Whitfield, P. S.; Kargina, I. *J. Electrochem. Soc.* **2002**, *149*, A176.
(24) Van der Ven, A.; Ceder, G. *J. Power Sources* **2001**, *97—98*, 529.
(25) Kang, K.; Ceder, G. *Phys. Rev. B* **2006**, *74*, 094105.
(26) Kang, K.; Meng, Y. S.; Bréger, J.; Grey, C. P.; Ceder, G. *Science* **2006**, *311*, 977.
(27) Thackeray, M. M.; Kang, S. H.; Johnson, C. S.; Vaughey, J. T.; Benedek, R.; Hackney, S. A. *J. Mater. Chem.* **2007**, *17*, 3112.
(28) Wen, J. G.; Bareño, J.; Lei, C. H.; Kang, S. H.; Balasubramanian, M.; Petrov, I.; Abraham, D. P. *Solid State Ionics* **2011**, *182*, 98.
(29) Kraft, S.; Stümpel, J.; Becker, P.; Kuetgens, U. *Rev. Sci. Instrum.* **1996**, *67*, 681.
(30) Zuo, J. M.; Mabon, J. C. . *Microsc. Microanal.* **2004**, *10* (Suppl. 2), 1000. (URL: http://emaps.mrl.uiuc.edu/)
(31) Nellist, P. D.; Pennycook, S. J. *Advances in Imaging and Electron Physics* **2000**, *113*, 147.
(32) Zabinsky, S. I.; Rher, J. J.; Ankudinov, A.; Eller, M. J. *Phys. Rev. B* **1995**, *52*, 2995.
(33) Meng, Y. S.; Ceder, G.; Grey, C. P.; Yoon, W.-S.; Shao-Horn, Y. *Electrochem. Solid State Lett.* **2004**, *7*, A115.
(34) Shao-Horn, Y.; Hackney, S. A.; Johnson, C. S.; Kahaian, A. J.; Thackeray, M. M. *J. Solid State Chem.* **1998**, *140*, 116.
(35) Shao-Horn, Y.; Hackney, S. A.; Armstrong, A. R.; Bruce, P. G.; Gitzendanner, R.; Johnson, C. S.; Thackeray, M. M. *J. Electrochem. Soc.* **1999**, *146*, 2404.
(36) Shao-Horn, Y.; Hackney, S. A.; Kahaian, A. J.; Thackeray, M. M. *J. Solid State Chem.* **2002**, *168*, 60.
(37) Kim, J.-S.; Johnson, C. S.; Vaughey, J. T.; Thackeray, M. M. *Chem. Mater.* **2004**, *16*, 1996.
(38) Lei, C. H.; Bareño, J.; Wen, J. G.; Petrov, I.; Kang, S.-H.; Abraham, D. P. *J. Power Sources* **2008**, *178*, 422.
(39) Bareño, J.; Lei, C. H.; Wen, J. G.; Kang, S.-H.; Petrov, I.; Abraham, D.P.. *Adv. Mater.* **2010**, *22*, 1122.
(40) Thackeray, M. M.; Kang, S.-H.; Johnson, C. S.; Vaughey, J. T.; Hackney, S. A. *Electrochem. Commun.* **2006**, *8*, 1531.
(41) Peres, J. P.; Weill, F.; Delmas, C. *Solid State Ionics* **1999**, *116*, 19.
(42) Boulineau, A.; Croguennec, L.; Delmas, C.; Weill, F. *Solid State Ionics* **2009**, *180*, 1652.
(43) Kikkawa, J.; Akita, T.; Tabuchi, M.; Shikano, M.; Tatsumi, K.; Kohyama, M. *J. Appl. Phys.* **2008**, *103*, 104911.
(44) Kikkawa, J.; Akita, T.; Tabuchi, M.; Shikano, M.; Tatsumi, K.; Kohyama, M. *J. Electrochem. Soc.* **2009**, *156*, A839.
(45) Luo, W.; Li, X.; Dahn, J. R. *J. Electrochem. Soc.* **2010**, *157*, A993.
(46) Zeng, D.; Cabana, J.; Bréger, J.; Yoon, W.-S.; Grey, C. P. *Chem. Mater.* **2007**, *19*, 6277.
(47) Kang, S.-H.; Abraham, D. P.; Yoon, W.-S.; Nam, K.-W.; Yang, X.-Q. *Electrochim. Acta* **2008**, *54*, 684.